**Tunable Electrical Conductivity in Metal-Organic Framework Thin-Film Devices**

**Authors:** A. Alec Talin[1,2*,] Andrea Centrone[2,3], Alexandra C. Ford$_1$, Michael E. Foster[1], Vitalie Stavila1, Paul Haney[2], R. Adam Kinney[2,3], Veronika Szalai[2], Farid El Gabaly[1], Heayoung P. Yoon[2,3], François Léonard[1], Mark D. Allendorf[1*]

**Affiliations:**

[1]Sandia National Laboratories, Livermore, CA 94551.

[2]Center for Nanoscale Science and Technology, National Institute of Standards and Technology, Gaithersburg, MD 20899.

[3]Maryland Nanocenter, University of Maryland, College Park, MD 20742 (USA).

*Correspondence to: aatalin@sandia.gov; mdallen@sandia.gov

**Abstract**:

We report a strategy for realizing tunable electrical conductivity in metal-organic frameworks (MOFs) in which the nanopores are infiltrated with redox-active, conjugated guest molecules. This approach is demonstrated using thin-film devices of the MOF $Cu_3(BTC)_2$ (also known as HKUST-1; BTC, benzene-1,3,5-tricarboxylic acid) infiltrated with the molecule 7,7,8,8-tetracyanoquinododimethane (TCNQ). Tunable, air-stable electrical conductivity over six orders of magnitude is achieved, with values as high as 7 Siemens per meter. Spectroscopic data and first-principles modeling suggest that conductivity arises from TCNQ guest molecules bridging the binuclear copper paddlewheels in the framework leading to strong electronic coupling between the dimeric Cu subunits. These ohmically conducting porous MOFs could have applications in conformal electronic devices, reconfigurable electronics, and sensors.

**Main Text**

MOFs (*1-3*) are crystalline materials with a nanoporous, supramolecular structure consisting of metal ions connected by multitopic organic ligands. These materials are typically poor electrical conductors because of the insulating character of the organic ligands and poor overlap between their π orbitals and the d orbitals of the metal ions. Combining the crystalline order of

MOFs with an ability to conduct electrical charge has the potential to create a new class of materials that would open applications such as conformal electronic devices, reconfigurable electronics, and sensors. Although strategies to engineer electrically conducting MOFs have been proposed (e.g., the use of second- or third-row transition metals, redox-active linkers, and hetero-bimetallic structures), few of these approaches have been realized (*4*). Until recently, only one example of an intrinsically conducting framework with permanent porosity was known, a p-type semiconducting MOF in which conductivity occurs via a redox mechanism (*5*). Very recently, Gandara *et al.* described a series of metal triazolate MOFs, one of which exhibits ohmic conductivity (*6*). The mechanism of conductivity in that case is not known, but it appears to be highly specific to the presence of Fe(II) in the structure, as MOFs in this series with the same structure but different divalent metals are not conducting. Importantly, there have been no reports of conducting MOF thin-film devices.

An alternative approach is to use the MOF pores themselves as a venue for modulating the electrical transport properties. We reasoned that infiltrating MOFs having open metal sites with molecules capable of charge transfer that can coordinate to these sites would create a mechanism for carrier mobility. Binuclear Cu(II) paddlewheel MOF structures, such as $Cu_3(BTC)_2$ (*7*) (also known as HKUST-1), are attractive candidates for testing this strategy. The coordination positions located on opposite ends of the Cu(II) axis of the paddlewheel, which are occupied by solvent (often water) in the as-synthesized material, can be exchanged with redox-active molecules such as TCNQ. Moreover, electron paramagnetic resonance (EPR) spectra suggest a somewhat delocalized electronic structure enabled by additional spin exchange among the copper dimers, which results from the carboxylates interconnecting the paddlewheel subunits (*8*).

Here, we describe the realization of this strategy using a thin-film device comprised of $Cu_3(BTC)_2$ (*7*) grown on electrodes and demonstrate control of ohmic electrical conductivity over six orders of magnitude. Silicon wafers covered with 100 nm of $SiO_2$ were pre-patterned with 100 nm-thick Pt pads (dimensions of 800 μm by 400 μm) and gaps of 100 μm, 150 μm, and 200 μm. $Cu_3(BTC)_2$ films with 100 nm nominal thickness were grown on the wafers from the liquid phase, as described previously (*9*). Grazing incidence XRD measurements and SEM imaging (Fig. 1, B and C) indicate a polycrystalline $Cu_3(BTC)_2{\cdot}xH_2O$ film with preferred orientation along the (111) direction (*10*). Current-voltage (I-V) characteristics obtained on as-

grown thin-film devices in air (Fig. 2A) exhibited very low conductivity (~ $10^{-6}$ S/m), consistent with the expected insulating nature of $Cu_3(BTC)_2$.

The as-grown films were infiltrated with TCNQ by first heating in vacuum at 190 ºC for 30 min to remove coordinated water molecules, then immediately transferred to a saturated TCNQ/$CH_2Cl_2$ solution. I-V curves for four such devices after 72 hours of exposure to the TCNQ solution [Fig. 2A and supplemental online materials (*11*)]. The infiltration led to dramatic increases in current, with a linear I-V curve and conductivity of 7 S/m, six orders of magnitude greater than the un-infiltrated device. Measurements as a function of channel length (Fig. 2B) revealed a monotonic increase in resistance with increasing electrode separation. The TCNQ-infiltrated devices were stable in ambient up to at least 40 days (Fig. 2C). The conductivity increases with temperature (Fig. 2, D and E), following a thermally activated relation $\sigma \sim \exp(E_a/T)$ with a low activation energy $E_a$ of 41±1 meV, similar to values reported for high-mobility organic polymeric semiconductors such as poly-3-hexylthiophene (P3HT) (*12*).

In contrast to previously reported, non-porous conducting coordination polymers, such as CuTCNQ (*12-15*), we could tune the device conductivity by changing the TCNQ exposure time. As seen in Fig. 2F, conductivity variation over several orders of magnitude was achievable. Furthermore, the increase in conductivity could be described by classic percolation theory (black solid line) (*16*), suggesting that TCNQ forms localized conducting regions, rather than acting as a dopant.

Chemical and physical characterization of MOF films and powders exposed to TCNQ verify that TCNQ resides in the MOF pores without altering the MOF crystal structure. Powder XRD patterns of as-synthesized $Cu_3(BTC)_2 \cdot xH_2O$, $Cu_3(BTC)_2$ (activated), and $Cu_3(BTC)_2$ infiltrated with TCNQ [hereafter TCNQ@ $Cu_3(BTC)_2$] showed that the MOF crystalline structure (face-centered cubic ) was unaffected by the infiltration process (Figs. 1B, S2) (*7*). Rietveld refinement yielded lattice parameters of 2.617 nm ± 0.001 nm and 2.635 nm ± 0.001 nm for $Cu_3(BTC)_2$ and TCNQ@ $Cu_3(BTC)_2$ powders, respectively. The peak at $2\theta=5.759°$ seen in the patterns of both $Cu_3(BTC)_2 \cdot xH_2O$ and TCNQ@$Cu_3(BTC)_2$ (but absent from that of activated MOF) is diagnostic for guest molecule binding to the open metal sites in the large pores, and indicates long range order *(17)*. The surface area of the activated $Cu_3(BTC)_2$ powder, obtained from $N_2$ adsorption isotherms using the Brunauer, Emmett, and Teller (BET) method, is 1844 $m^2$ g-1 ± 4 $m^2$ $g^{-1}$. This

value is typical of high-quality $Cu_3(BTC)_2$ 3*Fm_m* material with little or no pore collapse or residual reactant (*18*). After infiltration and drying in air, the TCNQ@$Cu_3(BTC)_2$ material displays a BET surface area of 214 $m^2$ g-1 ± 0.5 $m^2$ $g^{-1}$, suggesting high TCNQ loading. This result is confirmed by elemental analysis indicating a $Cu_3(BTC)_2$:TCNQ ratio of 2 based on carbon, nitrogen, and hydrogen content. This corresponds to about 8 TCNQ molecules per unit cell or 1 TCNQ molecule per MOF pore. The presence of nitrogen in the TCNQ@$Cu_3(BTC)_2$ films was further corroborated by x-ray photoelectron spectroscopy (XPS) (Fig. S3). Furthermore, visual examination of the powdered MOFs reveals the expected turquoise-blue color for the as-synthesized material and the violet-blue hue for the activated (dehydrated) MOF (Fig. S1). Upon exposure to TCNQ, the color of the crystals changes to teal, indicating a perturbation of the MOF electronic structure. The color of TCNQ@$Cu_3(BTC)_2$ does not change upon exposure to air (Fig. S1), suggesting that TCNQ is not displaced by atmospheric water vapor; XPS also showed a significantly lower oxygen concentration in the infiltrated specimen (Fig. S3) consistent with reduced water occupation of the pores. In contrast, the color of the activated MOF prior to TCNQ infiltration reverts almost instantly to that of the as-synthesized (hydrated) material when exposed to atmospheric moisture.

The realization of these new hybrid electronic materials raises a question concerning the nature of the interaction between the framework and TCNQ and the mechanism of charge transport. We probed the TCNQ/MOF interaction several ways. Ultraviolet-visible (UV-Vis) spectra were collected from films of the uninfiltrated $Cu_3(BTC)_2 \cdot xH_2O$, TCNQ@$Cu_3(BTC)_2$, and TCNQ in dilute solution. The absorption spectrum of the TCNQ@$Cu_3(BTC)_2$ film (Fig. 3A) exhibits the expected MOF peak at 340 nm, a peak at 410 nm associated with neutral TCNQ,(*18*), and broad new absorption bands centered at ~700 nm and ~850 nm that are absent in both $Cu_3(BTC)_2 \cdot xH_2O$ and TCNQ in $CH_2Cl_2$. These additional bands are well-known signatures for charge transfer (*13, 19*). Note that reacting either copper acetate or copper sulfate with TCNQ in methanol generated no precipitates or new absorption bands, indicating that confinement in the MOF pore is essential to the formation of a charge transfer complex between Cu(II) and TCNQ. TCNQ complexes have been characterized extensively by vibrational spectroscopies, where the frequencies of C=C and C≡N stretching modes are particularly sensitive to the extent of charge transfer (*13, 20, 21*). Raman spectra of TCNQ@$Cu_3(BTC)_2$ (Fig. 3B) indicate that the TCNQ C=C stretching frequency shifted from 1456 $cm^{-1}$ to 1437 $cm^{-1}$ and new peaks appeared at 1352 $cm^{-1}$ and 1296

$cm^{-1}$, a strong indication that TCNQ interacts with the available coordination sites on the $Cu^{2+}$ ions in the framework. A shift of 19 $cm^{-1}$ for the C=C wing stretching mode suggests a partial charge transfer of ~0.3$e^-$ between the framework and TCNQ(*20*). The nitrile stretch at 2229 $cm^{-1}$ is split into two peaks at 2226 $cm^{-1}$ and 2213 $cm^{-1}$ (see inset), indicating two non-equivalent C≡N bonding environments, in close agreement with our calculated vibration spectra *(11)*. IR spectra (Fig. 3C) also show that the C≡N stretch of TCNQ is affected by adsorption into the framework with a shift from 2223 $cm^{-1}$ to 2204 $cm^{-1}$ accompanied by significant peak broadening. According to Chappell *et al.* (*21*), this shift corresponds to a charge transfer of ~0.4e- between the framework and TCNQ, in reasonable agreement with the value inferred from the Raman spectra. The observation of partial charge transfer is further supported by room temperature EPR spectra obtained from TCNQ@$Cu_3(BTC)_2$ (Fig. 3D), which display no evidence of TCNQ radical anions (*22*). Partial charge transfer is characteristic of many conducting TCNQ salts; however, in contrast to the well-studied CuTCNQ, in which Cu(+1) predominates, Cu in $Cu_3(BTC)_2$ remains in (+2) state after infiltration, as revealed by XPS (Fig. S4).

The importance of guest/host interactions was further probed by replacing TCNQ with its fully hydrogenated counterpart, H4-TCNQ (cyclohexane-1,4-diylidene)dimalononitrile), which lacks a conjugated π electron network, and F4-TCNQ (2,3,5,6-tetrafluoro-7,7,8,8-tetracyanoquinodimethane), which has a similar HOMO-LUMO gap but higher electron affinity compared to TCNQ. Elemental analysis indicates that the loading of H4-TCNQ is similar to that of TCNQ, i.e., about 1 H4-TCNQ molecule per pore. The I-V curve (Fig. 2A) for H4-TCNQ@$Cu_3(BTC)_2$ is essentially the same as the uninfiltrated, non-conducting MOF. The UV-Vis spectrum also lacks the characteristic bands indicative of charge transfer in TCNQ@ $Cu_3(BTC)_2$ (Fig. 3A). These results illustrate that the availability of guest molecule orbitals that can accept charge, as is the case in TCNQ but not H4-TCNQ, is important for achieving high conductivity. F4-TCNQ@ $Cu_3(BTC)_2$ is not as conductive as TCNQ@$Cu_3(BTC)_2$. We view this result as semi-quantitative, however, because F4-TCNQ is volatile and unlike TCNQ@ $Cu_3(BTC)_2$, the conductivity was not stable with time. Nevertheless, the lower conductivity measured immediately after infiltration suggests that the high electron affinity of this molecule inhibits electron mobility.

Finally, ab initio calculations suggest a possible mechanism for the appearance of conductance in TCNQ@ $Cu_3(BTC)_2$ hybrids. As illustrated in Fig. 3E, the calculations predict that TCNQ

binds strongly to the MOF (binding energy of 83.9 kJ/mol) and four such molecules create a continuous path through the unit cell (Fig. 3F and Movie S1). Furthermore, our calculations using molecular clusters comprised of two copper dimer groups (MOF SBUs) bridged by a TCNQ molecule show that: 1) the bridging TCNQ inserts unoccupied molecular orbitals into the MOF HOMO-LUMO gap (Fig. S5 and discussion), producing the new charge transfer band in the visible and enabling electronic coupling between the MOF and TCNQ. 2) Computed values of *H*AB, the electronic coupling matrix element for electron transfer from the MOF cluster to TCNQ (i.e. $TCNQ@Cu_3(BTC)_2^- \rightarrow TCNQ^-@Cu_3(BTC)_2$)), combined with the value of $\Delta G^*$ obtained from the temperature dependence of the conductivity, allow us to evaluate the extent of donor-acceptor coupling using the quantity $2H_{AB}/\lambda$ defined by Brunschwig *et al.* ($\lambda$ is the reorganization parameter) (*19*). We find $2H_{AB}/\lambda = 1.21$ for $TCNQ@Cu_3(BTC)_2$, identifying this material as a Class III system according to the Robin-Day classification scheme *(19*). These calculations also predict that electronic coupling in F4-$TCNQ@Cu_3(BTC)_2$ is intermediate between H4-TCNQ and TCNQ itself. The order of *H*AB values is H4-TCNQ < F4-TCNQ < TCNQ (0.19 eV < 1.03 eV < 2.32 eV), a trend that is consistent with the observed conductivities.

**References and Notes:**


1. O. M. Yaghi *et al.*, *Nature* **423**, 705 (Jun, 2003).
2. S. Shimomura and S. Kitagawa, *J. Mater. Chem.*, 21, 5537 (2011).
3. G. Ferey, *Chem. Soc. Rev.* **37**, 191 (2008).
4. C. H. Hendon, D. Tiana, A. Walsh, *Phys. Chem. Chem. Phys.* **14**, 13120 (2012).
5. Y. Kobayashi, B. Jacobs, M. D. Allendorf, J. R. Long, *Chem. Mater.* **22**, 4120 (Jul, 2010).
6. F. Gandara *et al.*, *Chem. Eur. J.* **18**, 10595 (Aug, 2012).
7. S. S. Y. Chui, S. M. F. Lo, J. P. H. Charmant, A. G. Orpen, I. D. Williams, *Science* **283**, 1148 (Feb, 1999).
8. A. Poppl, S. Kunz, D. Himsl, M. Hartmann, *J. Phys. Chem. C* **112**, 2678 (Feb, 2008).
9. V. Stavila, J. Volponi, A. M. Katzenmeyer, M. C. Dixon, M. D. Allendorf, *Chem. Sci.* **3**, 1531 (2012).
10. O. Shekhah, H. Wang, D. Zacher, R. A. Fischer, C. Woll, *Angew. Chem. Int. Ed.* **48**, 5038 (2009).
11. Supplementary online material.

12. L. R. Melby *et al.*, *J. Am. Chem. Soc.* **84**, 13 (1962).
13. R. A. Heintz *et al.*, *Inorg. Chem.* **38**, 13 (1999).
14. R. S. Potember, T. O. Poehler, D. O. Cowan, *Appl. Phys. Lett.* **34**, 405 (1979).
15. H. Miyasaka *et al.*, *J. Amer. Chem. Soc.* **132**, 13 (2010).
16. B. Abeles, H. L. Pinch, J. I. Gittleman, *Phys. Rev. Lett.* **35**, 247 (1975).
17. H. –C. Zhou et al. *J. Appl. Cryst.* 46, 346(2013)
18. L. H. Wee, M. R. Lohe, N. Janssens, S. Kaskel, J. A. Martens, *J. Mater. Chem.* **22**, 13742 (2012).
19. B. S. Brunschwig, C. Creutz, N. Sutin, *Chem. Soc. Rev.* **31**, 17 (2002).
20. S. Matsuzaki, R. Kuwata, K. Toyoda, *Sol. State Comm.* **33**, 3 (1980).
21. J. S. Chappell *et al.*, *J. Amer. Chem. Soc.* **103**, 2442 (1981).
22. G. Inzelt, R. W. Day, J. F. Klnstle, J. O. Chambers, *J. Phys. Chem.* **87**, 7 (1983).

**Acknowledgments:**
We thank S. T. Meek for organic synthesis in this work and D. Ruzmetov for help in fabrication. This work was supported by the Laboratory Directed Research and Development Program at Sandia National Laboratories and the U.S. DOE SunShot Program. Sandia is a multi-program laboratory operated by Sandia Corporation, a Lockheed Martin Company, for the U.S. DOE National Nuclear Security Administration under Contract DE-AC04-94AL85000. AAT was supported by the Science of Precision Multifunctional Nanostructures for Electrical Energy Storage (NEES), an Energy Frontier Research Center funded by the U.S. DOE, Office of Science, Office of Basic Energy Sciences under award DESC0001160. F.E.G. was supported by the Office of Basic Energy Sciences, Division of Materials and Engineering Sciences, U.S. DOE, under contract no. DE-AC04-94AL85000. A.C., R.A.K., and H.Y. acknowledge support under the Cooperative Research Agreement between the University of Maryland and the National Institute of Standards and Technology Center for Nanoscale Science and Technology, Award 70NANB10H193, through the University of Maryland.

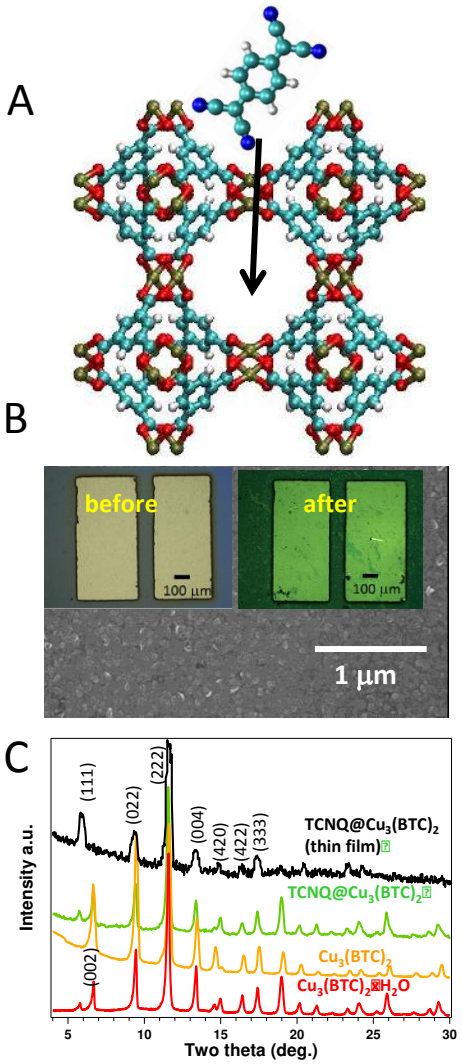


**Fig. 1**. Fabrication of conductive MOF thin-film devices and structural characterization. (**A**) TCNQ molecule shown above a $Cu_3(BTC)_2$ MOF; arrow points into the pore. White – hydrogen; blue – nitrogen; cyan – carbon; red – oxygen; light brown – copper. (B) SEM image of MOF-coated device, with optical images of devices before and after TCNQ infiltration. (C) XRD data for powders and grazing incidence XRD for a thin film.

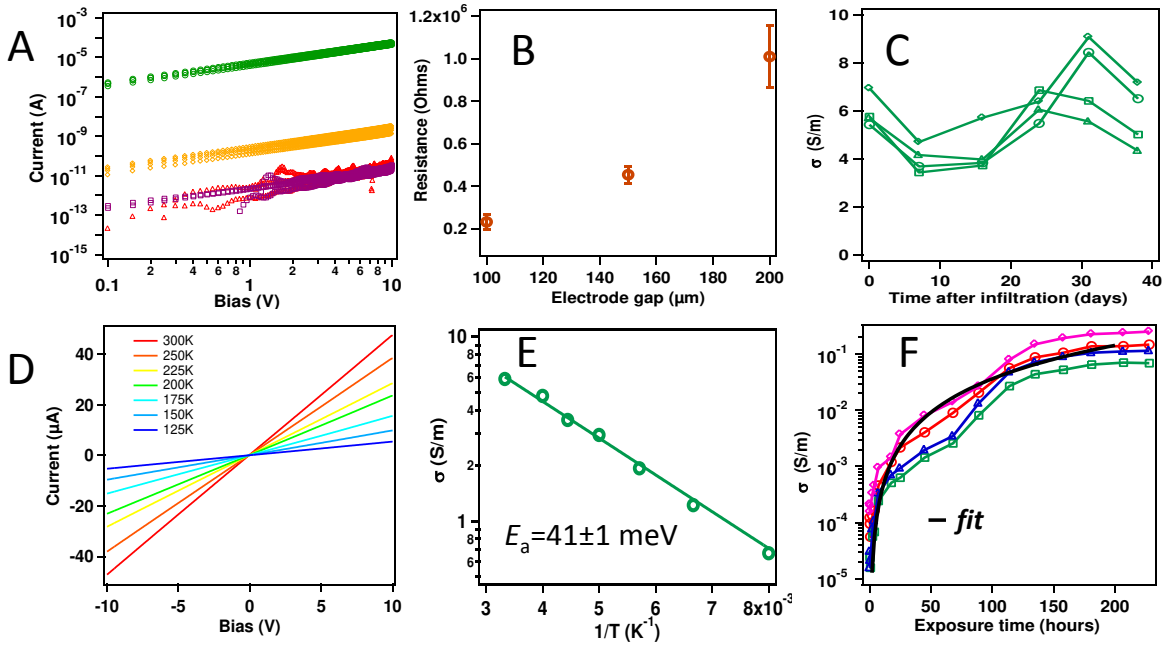


**Fig. 2**. Electronic transport characteristics of MOF thin-film devices. (**A**) I-V curves before (red) and after infiltration with: TCNQ (green); F4-TCNQ (gold); H4-TCNQ (purple). (**B**) Channel-length dependence of conductivity for TCNQ-infiltrated devices. (**C**) Stability of conductivity over time for several devices. (**D**) I-V curve temperature dependence. (**E**) Arrhenius plot of the conductivity. (**F**) Conductivity vs. exposure time for several devices. Black line: fit to percolation theory, $\sigma = 4\times10^{-6}\left(t-0.5\right)^2$ where $t$ is exposure time.

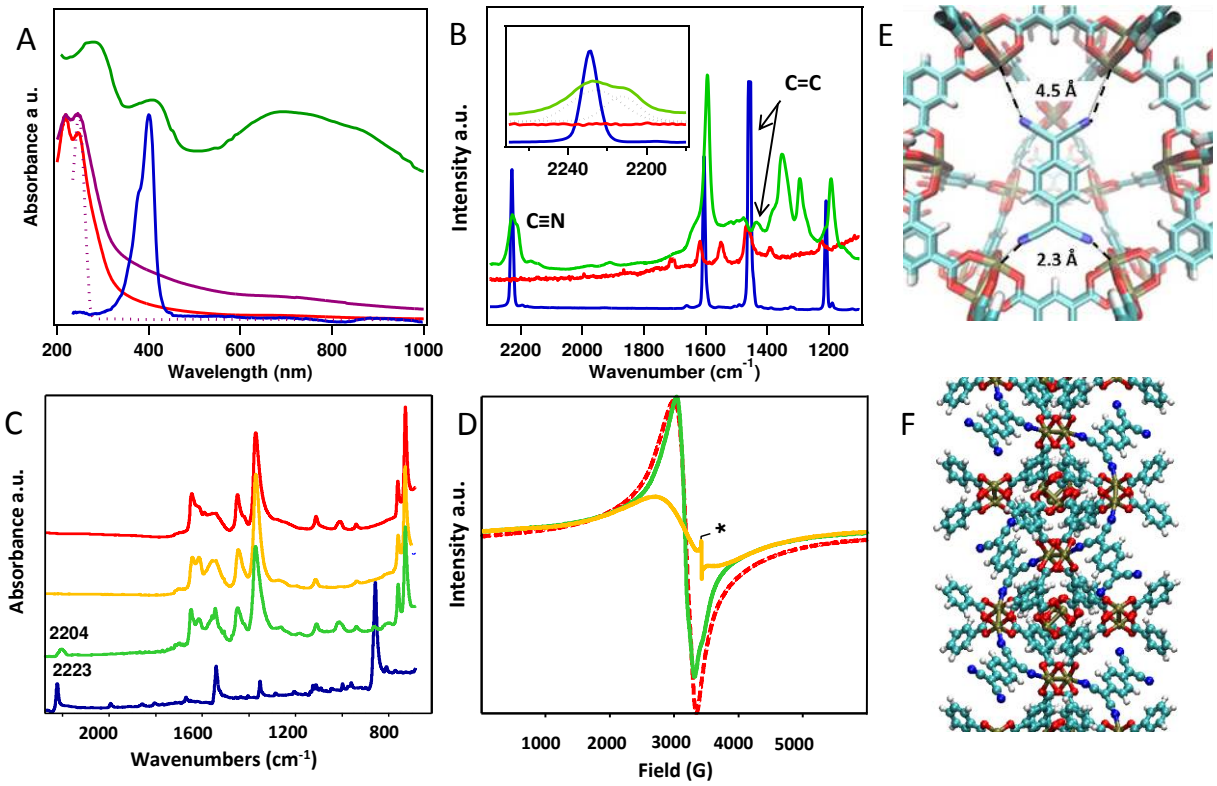


**Fig. 3.** Evidence for interaction between TCNQ and the MOF. **(A)** Transmission UV-Vis spectra collected for a $Cu_3(BTC)_2{\cdot}xH_2O$ film on borosilicate substrate before (red) and after adsorption with TCNQ (green) and H4-TCNQ (purple), and for TCNQ in methanol (blue); (**B**) Raman spectra collected for a $Cu_3(BTC)_2{\cdot}xH_2O$ film on borosilicate substrate before (red) and after adsorption of TCNQ (green), and for TCNQ crystals deposited onto a glass slide (blue); **(C)** infrared spectra collected for $Cu_3(BTC)_2{\cdot}xH_2O$ (red), $Cu_3(BTC)_2$ (yellow), TCNQ@$Cu_3(BTC)_2$ (green), and TCNQ powder (blue); **(D)** room temperature continuous wave EPR spectra of activated $Cu_3(BTC)_2$ (yellow), $Cu_3(BTC)_2$ stirred in methanol (red dashed), and $Cu_3(BTC)_2$ stirred in methanol containing TCNQ (green). The asterisk (*) denotes an unidentified organic radical signal observed only in the activated $Cu_3(BTC)_2$ sample. (**E**) Minimum energy configuration for TCNQ@$Cu_3(BTC)_2$ obtained from ab initio calculations. (**F**) Possible configuration that would provide a conductive channel through the MOF unit cell (atom color code for **E** and **F** as in Fig. 1).

# Supplementary Materials for

## Tunable Electrical Conductivity in Metal-Organic Framework Thin-Film Devices

A. Alec Talin,* Andrea Centrone, Alexandra C. Ford, Michael E. Foster, Vitalie Stavila, Paul Haney, R. Adam Kinney, Veronika Szalai, Farid El Gabaly, Heayoung P. Yoon, François Léonard, Mark D. Allendorf*

*Corresponding author. E-mail: aatalin@sandia.gov (A.A.T.); mdallen@sandia.gov (M.D.A.)

Published 5 December 2013 on *Science* Express
DOI: 10.1126/science.1246738

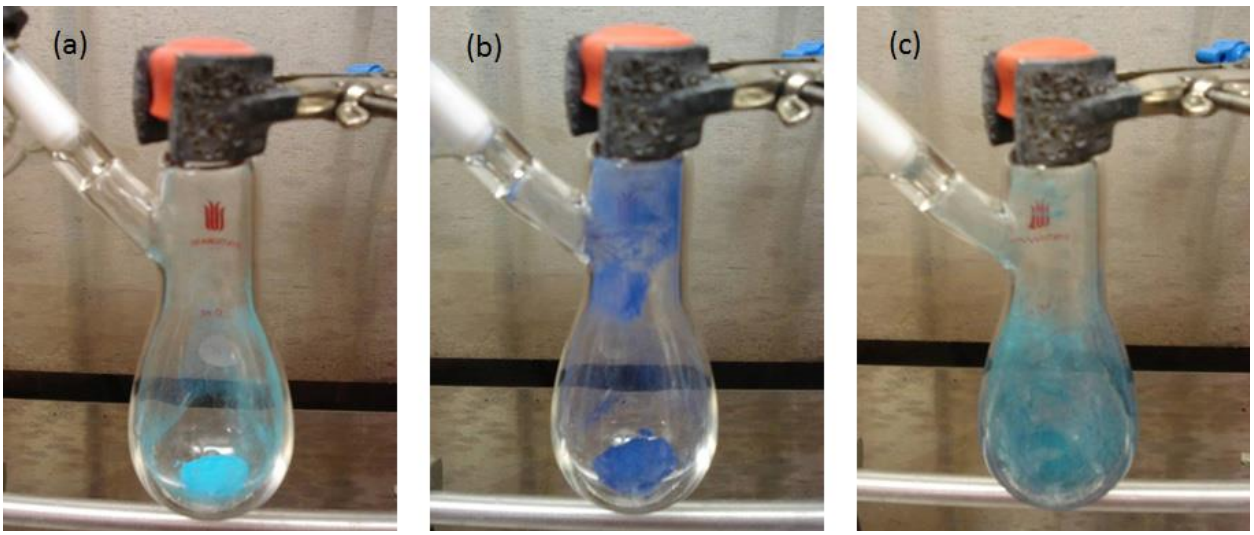


**Figure S1** (a) $Cu_3(BTC)_2 \cdot xH_2O$ powder (b) $Cu_3(BTC)_2$ obtained by heating to 180 °C for 30 min under vacuum (c) TCNQ@$Cu_3(BTC)_2$

**Elemental Analysis**

The elemental analysis (C, H, N, Cl) was performed by Columbia Analytical Services, Inc. For both TCNQ and H4-TCNQ infiltrated samples the best match was obtained for a TCNQ (H4-TCNQ) : $Cu_3(BTC)_2$ ratio of 1:6. In order to estimate the loading per large MOF pore, we first determined the loading per single $Cu_3(BTC)_2$ unit cell to be 8 TCNQ or H4-TCNQ molecules. Since each $Cu_3(BTC)_2$ unit cell contains 8 large pores and 48 copper atoms (from the CIF-file), this corresponds to a loading of approximately one TCNQ or H4-TCNQ molecule per MOF pore.

| **Sample** | Carbon, % | | Hydrogen, % | | Nitrogen, % | |
|---|---|---|---|---|---|---|
| | Exp. | Calc. | Exp. | Calc. | Exp. | Calc. |
| $TCNQ@Cu_3(BTC)_2$<br>$1TCNQ:2Cu_3(BTC)_2$ | 40.21 | 40.43 | 1.37 | 1.98 | 4.18 | 3.93 |
| $H4\text{-}TCNQ@Cu_3(BTC)_2$*<br>$1TCNQ:2Cu_3(BTC)_2:1/3CH_2Cl_2$ | 39.72 | 39.81 | 2.04 | 2.86 | 4.69 | 3.84 |

**Table S1:** Elemental analysis data.

* According to the elemental analysis the as-synthesized $H4\text{-}TCNQ@Cu_3(BTC)_2$ powder also contains chlorine, presumable from residual solvent present in the MOF pores (Calc. (%) Cl for $1TCNQ:2Cu_3(BTC)_2:1/3CH_2Cl_2$ 1.62, found 1.3).

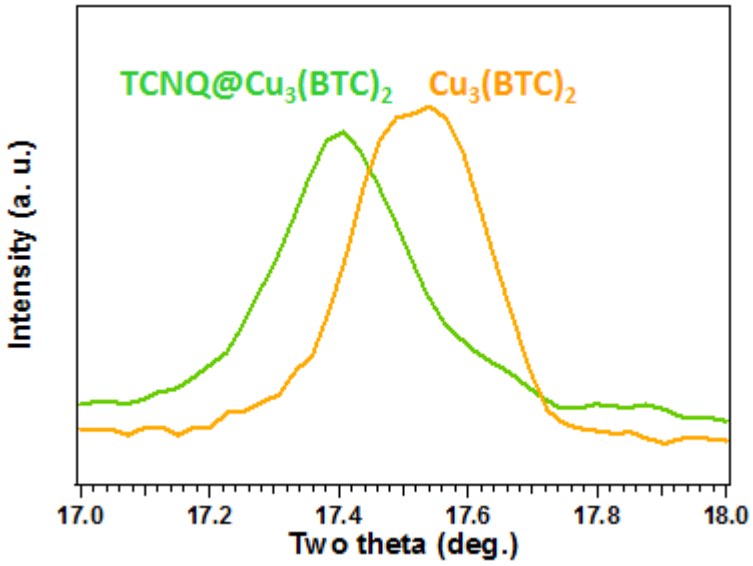


**Figure S2**. $Cu_3(BTC)_2$ (333) reflection before and after infiltration showing a shift to lower angle indicating slight lattice expansion after adsorption of TCNQ (see main text for calculated lattice parameters)

## X-ray photoelectron spectroscopy (XPS)

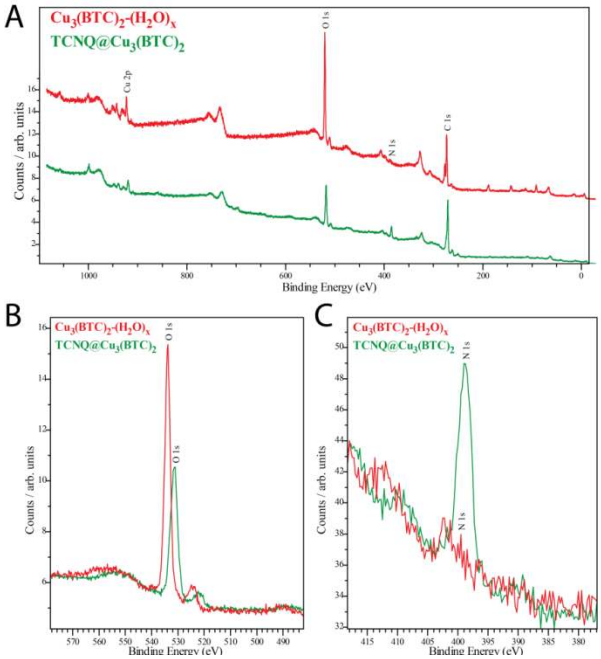


**Figure S3**. A) XPS survey spectra showing the surface composition of $Cu_3(BTC)_2$-$(H_2O)_x$ and TCNQ@$Cu_3(BTC)_2$ films under similar conditions. Both specimens were held in laboratory air for several weeks. The spectra have not been corrected or processed. Core level peaks of the main components have been labeled. B) lower O concentration for TCNQ@$Cu_3(BTC)_2$ is consistent with lower $H_2O$ concentration in infiltrated MOF films. C) a prominent N peak is present in spectrum of TCNQ@$Cu_3(BTC)_2$ compared to virtually no N in $Cu_3(BTC)_2$-$(H_2O)_x$. Note the slight (2.74 eV) shift in binding energy for $Cu_3(BTC)_2$-$(H_2O)_x$ due to charging. No charging is observed for TCNQ@$Cu_3(BTC)_2$.

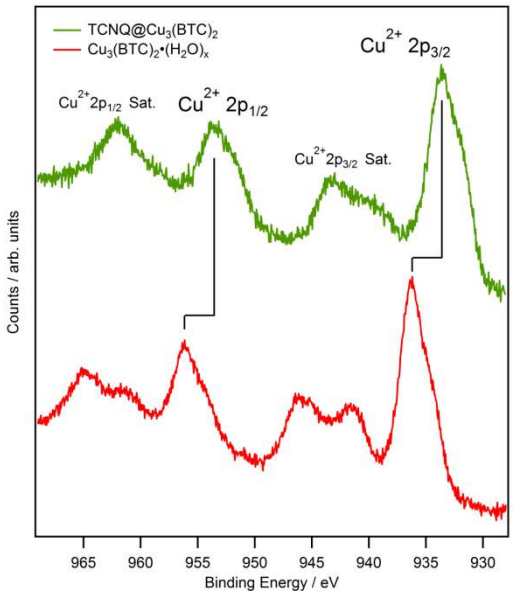


**Figure S4**: Cu 2p XPS spectra of the $Cu_3(BTC)_2$-$(H_2O)_x$ (red line) and TCNQ@$Cu_3(BTC)_2$ (green). Both spectra show clear features representative of $Cu^{2+}$ oxidation states(*27*). Note the shift of +2.74 eV in binding energy due to charging in the spectrum of $Cu_3(BTC)_2$-$(H_2O)_x$ due to its limited electronic conductivity.

## Computational Methods

All molecular orbital calculations on molecules and clusters were carried out with an open source simulation package (NWChem) *(24)* using the spin-unrestricted DFT formalism with the B3LYP exchange-correlation functional (UB3LYP) *(25)* and the Ahlrich triple-zeta valence basis set with polarization on all atoms (TZVP) *(26)*. The broken-symmetry (BS) approach *(27, 28)* was applied, which was required for the correct ordering the electronic states (singlet state < triplet state). No constraints were applied to the atoms' positions during the geometry optimizations and all default convergence criteria were used.

Full geometry optimizations were performed on TCNQ, F4-TCNQ, H4-TCNQ and corresponding $Cu_3(BTC)_2$ representative molecular clusters (TCNQ@$Cu_3(BTC)_2$, F4-TCNQ@$Cu_3(BTC)_2$, H4-TCNQ@$Cu_3(BTC)_2$ and $H_2O$ @CuBTC). These calculations allowed us to ascertain the location and energy of highest occupied molecular orbitals (HOMO) and the lowest unoccupied molecular orbitals (LUMO). The HOMO/LUMO orbital energies of $H_2O$@CuBTC (a representation of the MOF before infiltration), TCNQ, F4-TCNQ and H4-TCNQ are schematically shown in Figure S5. This figure clearly indicates that the LUMO of TCNQ and F4-TCNQ lies within the bandgap of the MOF; therefore, upon infiltration a new metal-to-ligand charge transfer (MLCT) state is created. However, H4-TCNQ possesses a large bandgap and does not perturb the frontier orbitals of the MOF. The HOMO/LUMO and corresponding orbital energies of TCNQ@$Cu_3(BTC)_2$ and $H_2O$ @CuBTC are shown in Fig. S6. This figure clearly show that the LUMO moves from the MOF to TCNQ upon infiltration effectively reducing the bandgap of the material; whereas, the HOMO is relatively unchanged by the addition of TCNQ. The frontier molecular orbitals provide evidence that upon infiltration of TCNQ a new MLCT and/or LLCT state is created. This result is in agreement with the experimentally UV/Vis spectrum, where a new absorption peak around 700 nm is observed. A Lowdin population analysis of the ground state was also preformed revealing that electron density is transferred from TCNQ to $Cu_3(BTC)_2$; this was determined by summation of the partial atomic charges on TCNQ resulting in a charge of +0.20.

To help assign and explain the experimentally observed splitting of the C≡N stretch of TCNQ upon infiltration, the vibrational frequency of TCNQ and the TCNQ@$Cu_3(BTC)_2$ cluster were determined at the B3LYP/DZVP level of theory (see Fig. S7). Experimentally, the nitrile stretch of TCNQ at 2229 $cm^{-1}$ is split into two peaks at 2226 $cm^{-1}$ and 2213 $cm^{-1}$ upon infiltration into the MOF. This suggests that there are two non-equivalent C≡N bonds which are hypothesized to be a result of TCNQ binding to the Cu-paddlewheels. The same splitting is observed in the predicted IR active modes corresponding to C≡N stretches. For TCNQ, a single C≡N stretch is predicted at 2317 $cm^{-1}$ and is split into two IR active modes at 2317 $cm^{-1}$ and 2348 $cm^{-1}$ when bound to the $Cu_3(BTC)_2$ cluster. The predicted splitting is in good agreement with experiment confirming that TCNQ is bound to the Cu-paddlewheels.

The electronic coupling for the transfer of an electron from the MOF cluster to the bound TCNQ/F4-TCNQ/H4-TCNQ molecule has been calculated using Hartree-Fock exchange within the constrained density functional theory (CDFT) formalisum *(29)*. For each system an electron (-1 charge) was constrained to the respective units (e.g. TCNQ@$Cu_3(BTC)_2$ $^-$ → TCNQ$^-$@$Cu_3(BTC)_2$). The electronic matrix coupling element ($H_{ab}$) was computed between the two diabetic states using the method of *Corresponding Orbital Transformation* as implemented in NWCHEM *(30)*. The resulting order of the $H_{AB}$ values is H4-TCNQ < F4-TCNQ < TCNQ (0.19 eV < 1.03 eV < 2.32 eV), a trend that is consistent with the observed conductivities. It is recognized that the magnitude of the coupling may be large; however, the trend provides qualitative evidence that the experimentally observed conductivity is a result of increased

electronic coupling. Moreover, an increase in electronic coupling corresponds to an increase in mobility in accordance with Marcus theory *(31)*.

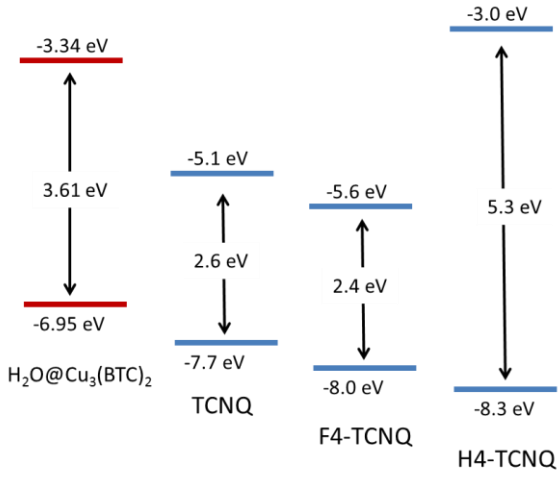


**Figure S5**: A schematic representation of the alignment of the HOMO/LUMO orbitals and bandgaps of $H_2O$@CuBTC, TCNQ, F4-TCNQ, and H4-TCNQ determined at the UB3LYP/VTZP level of theory.

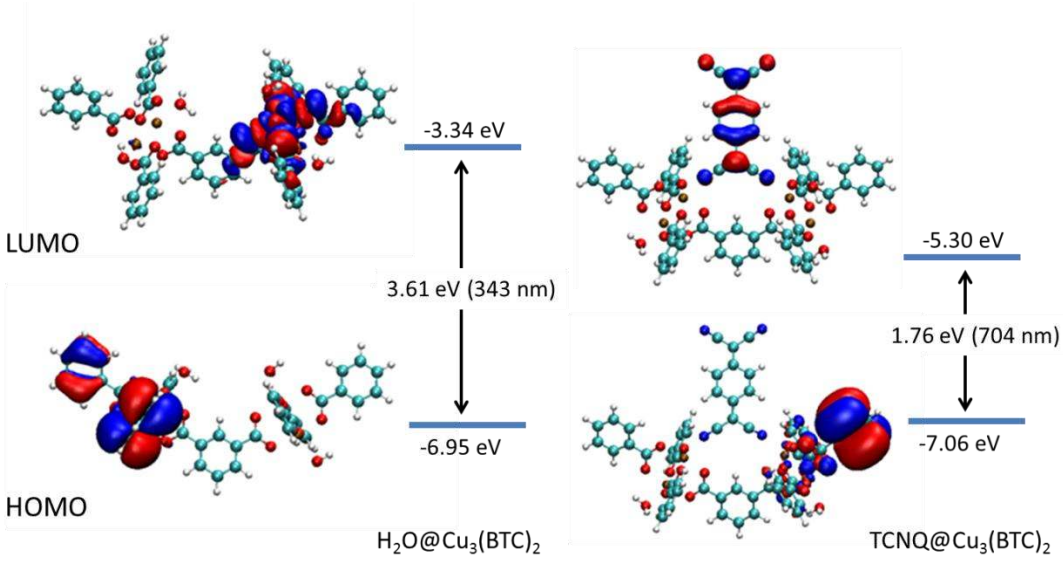


**Figure S6**: The HOMO/LUMO isosurfaces and orbital energies of the UB3LYP/VTZP optimized molecular clusters. Left – the molecular cluster and with water only. Right - the molecular cluster with waters and TCNQ.

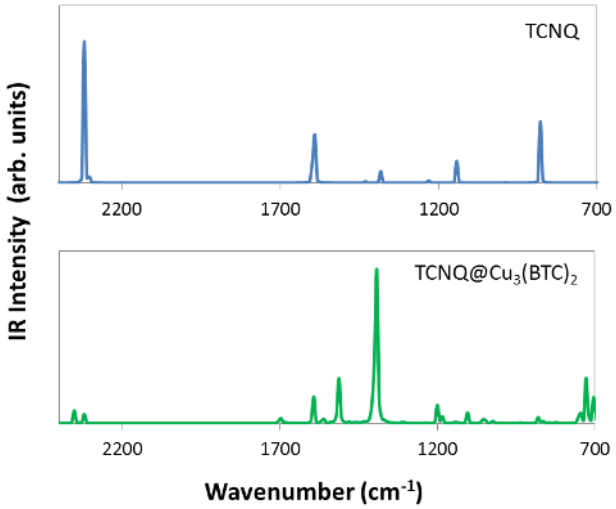


**Figure S7**: The B3LYP/DZVP predicted IR spectrum for TCNQ (top) and the TCNQ@$Cu_3(BTC)_2$ cluster (bottom). The spectra were created by Gaussian convolution about the IR active vibrational modes with a FWHM of 3 $cm^{-1}$.

A commercial ab initio simulation package (VASP) *(32-35)* (*27-30*) was used for the periodic boundary condition (PBC) calculation of TCNQ@ $Cu_3(BTC)_2$ using the PBEsol functional *(36)* (a revised Perdew-Burke-Ernzerhof (PBE) GGA functional) with an energy cutoff of 500 eV. The projector-augmented-wave (PAW)*(37,38).* pseudo-potentials were used to describe the interactions between the ions and electrons. A gamma-point was used for sampling the Brillouin zone due to the size of the system (784 atoms). During the structural optimization the $Cu_3(BTC)_2$ framework was fixed (atoms positions and unit cell dimensions) and only the TCNQ molecules were optimized. This approximation was needed to reduce the required computational expense and is reasonable given the crystal structure of $Cu_3(BTC)_2$. A close-up of TCNQ binding to the Cu-paddlewheels, based on the DFT optimized geometry, is shown in Fig 3E.

Based on the elemental analysis, the loading of TCNQ in $Cu_3(BTC)_2$ was taken to be one TCNQ per large pore. $Cu_3(BTC)_2$ also contains a small pore; however, it is incapable of containing a TCNQ molecule. Upon inspection, two slightly different large pores can be identified and are referred to as *pore 1* and *pore 2*. In *pore 1* (Fig. 3E), the copper paddlewheels point in towards the pore cavity allowing TCNQ to bind directly to the Cu paddlewheels. In *pore 2* (not shown), the copper paddlewheels point away from the pore cavity hindering TCNQ from binding to the Cu paddlewheels. Therefore, it can be assumed that TCNQ is more strongly bound in *pore 1*. The distances between each nitrogen atom in TCNQ and the copper atoms in the optimized geometry are displayed in Fig. 3E; TCNQ is found to be within reasonable covalent binding distance of Cu atoms in *pore 1*, with the distance between the nitrogen atoms binding directly to Cu atoms being on average 2.3 Å.

The binding energy (BE) of TCNQ to $Cu_3(BTC)_2$ was determined from

$$BE = E_{total} - E_{TCNQ} + E_{MOF} \quad \text{(S1)}$$

where $E_{total}$ is the total energy of the optimized system, $E_{TCNQ}$ is the total energy of the isolated TCNQ molecule, and $E_{MOF}$ is the total energy of the MOF without TCNQ. The resulting binding

energy of TCNQ is 83.9 kJ/mol. In addition, a single TCNQ molecule was placed in a π-π stacking orientation with a linker within the framework and optimized. This calculation was carried out to help confirm that TCNQ prefers to bind and bridge the Cu-paddelwheels. In order to properly model this π-π stacking system an empirical van der Waal correction was incorporated in the DFT calculation as implemented in VASP. In addition, the same calculation was carried out with a single TCNQ placed in the conformation shown in Fig. 3E (bridging two Cu-paddlewheels). The calculations reveal that the bridging conformation is lower in energy by 25 kJ/mol. Upon inclusion of the empirical van der Waal correction term, the binding energy of the bridging complex increased to 111 kJ/mol.
Movie S1 depicting the organization of the TCNQ molecules that leads to a possible conducting path through the MOF unit cell is available online. The structural orientation is based on a 1D representation for which all the atom positions have been optimized at the same level of theory discussed above.

**Triplet state EPR signals**

The excited state triplet spectrum arising from the antiferromagnetically-coupled $Cu(II)_2$ dimer of the paddle-wheel subunits in $Cu_3(BTC)_2$ is shown in Figure S8, for each of the three samples. Only two of the four expected transitions for an axial symmetric complex, $H_{(x,y)1}$ and $H_{(x,y)2}$, are resolved at the microwave frequency used for our measurements (9.6 GHz) *(39)*. The triplet signal is most intense in the TCNQ@$Cu_3(BTC)_2$ and was simulated using the Hamiltonian (eq. S2)

$$\hat{H} = \beta_e \mathbf{g} \hat{S} + \hat{S}\mathbf{D} \quad \text{(S2)}$$

where **g** is the anisotropic electronic Zeeman interaction, and **D** is the zero-field splitting tensor (D = [$D_z$, $D_y$, $D_x$]): **g** = [2.369, 2.06, 2.06]; $D_z$ = 9550 MHz (0.318 $cm^{-1}$). The zero-field splitting ($D_z$) for the triplet in the TCNQ-treated sample (0.318 $cm^{-1}$) is almost identical to that obtained by Pöppl, et al for activated HKUST-1 (0.320 $cm^{-1}$). Because the zero field splitting for the $Cu(II)_2$ dimer should be influenced by both the inter-copper distance and by the copper spin density, we would predict a change in these parameters if TCNQ interacts strongly with all of the $Cu(II)_2$ dimer units. Coordination of TCNQ to a large majority of $Cu(II)_2$ units would break the centrosymmetry of the subunit, introducing rhombicity in the g tensor and modifying the triplet EPR spectrum of the TCNQ-treated $Cu_3(BTC)_2$ relative to the parent compound.

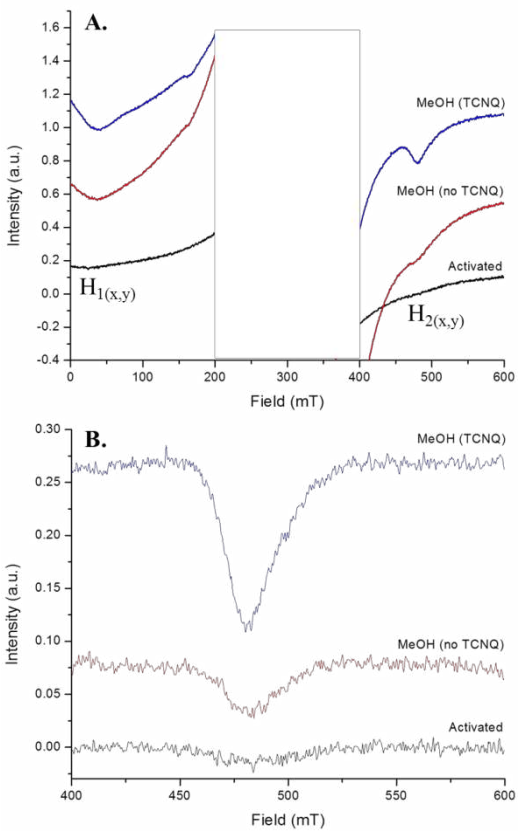


**Figure S8.** A) Low temperature (70 K) X-Band CW EPR spectra of the excited-state triplet for the antiferromagnetically coupled $Cu(II)_2$ subunit in activated (black), MeOH (red), and TCNQ-treated (blue) $Cu_3(BTC)_2$. The two additional transitions expected for a triplet described by an axial g tensor ($H_{1z}$ and $H_{2z}$) are not resolved. B) Baseline corrected CW EPR spectra of the $H_{2(x,y)}$ transition of the dimeric copper excited state triplet for the three samples.

## References

1. O. M. Yaghi, M. O'Keeffe, N. W. Ockwig, H. K. Chae, M. Eddaoudi, J. Kim, Reticular synthesis and the design of new materials. *Nature* **423**, 705–714 (2003).

2. S. Shimomura, S. Kitagawa, Soft porous crystal meets TCNQ: Charge transfer-type porous coordination polymers. *J. Mater. Chem.* **21**, 5537 (2011).

3. G. Férey, Hybrid porous solids: Past, present, future. *Chem. Soc. Rev.* **37**, 191–214 (2008).

4. C. H. Hendon, D. Tiana, A. Walsh, Conductive metal-organic frameworks and networks: Fact or fantasy? *Phys. Chem. Chem. Phys.* **14**, 13120–13132 (2012).

5. Y. Kobayashi, B. Jacobs, M. D. Allendorf, J. R. Long, Conductivity, doping, and redox chemistry of a microporous dithiolene-based metal-organic framework. *Chem. Mater.* **22**, 4120–4122 (2010).

6. F. Gándara, F. J. Uribe-Romo, D. K. Britt, H. Furukawa, L. Lei, R. Cheng, X. Duan, M. O'Keeffe, O. M. Yaghi, Porous, conductive metal-triazolates and their structural elucidation by the charge-flipping method. *Chemistry* **18**, 10595–10601 (2012).

7. S. S. Y. Chui, S. M. F. Lo, J. P. H. Charmant, A. G. Orpen, I. D. Williams, A chemically functionalizable nanoporous material. *Science* **283**, 1148–1150 (1999).

8. A. Poppl, S. Kunz, D. Himsl, M. Hartmann, CW and pulsed ESR spectroscopy of cupric ions in the metal-organic framework compound $Cu_3(BTC)_2$. *J. Phys. Chem. C* **112**, 2678–2684 (2008).

9. V. Stavila, J. Volponi, A. M. Katzenmeyer, M. C. Dixon, M. D. Allendorf, Kinetics and mechanism of metal-organic framework thin film growth: Systematic investigation of HKUST-1 deposition on QCM electrodes. *Chem. Sci.* **3**, 1531–1540 (2012

10. O. Shekhah, H. Wang, D. Zacher, R. A. Fischer, C. Woll, Growth mechanism of metal-organic frameworks: Insights into the nucleation by employing a step-by-step route. *Angew. Chem. Int. Ed.* **48**, 5038–5041 (2009).

11. See supplementary materials on *Science* Online.

12. L. R. Melby, R. J. Harder, W. R. Hertler, W. Mahler, R. E. Benson, W. E. Mochel, Substituted quinodimethans. II. Anion-radical derivatives and complexes of 7,7,8,8-tetracyanoquinodimethan. *J. Am. Chem. Soc.* **84**, 3374–3387 (1962).

13. R. A. Heintz, H. Zhao, X. Ouyang, G. Grandinetti, J. Cowen, K. R. Dunbar, New insight into the nature of Cu(TCNQ): Solution routes to two distinct polymorphs and their relationship to crystalline films that display bistable switching behavior. *Inorg. Chem.* **38**, 144–156 (1999).

14. R. S. Potember, T. O. Poehler, D. O. Cowan, Electrical switching and memory phenomena in Cu-TCNQ thin films. *Appl. Phys. Lett.* **34**, 405 (1979).

15. H. Miyasaka, N. Motokawa, S. Matsunaga, M. Yamashita, K. Sugimoto, T. Mori, N. Toyota, K. R. Dunbar, Control of charge transfer in a series of $Ru_2^{II,II}$/TCNQ two-dimensional networks by tuning the electron affinity of TCNQ units: A route to synergistic magnetic/conducting materials. *J. Am. Chem. Soc.* **132**, 1532–1544 (2010

16. B. Abeles, H. L. Pinch, J. I. Gittleman, Percolation conductivity in W-$Al_2O_3$ granular metal films. *Phys. Rev. Lett.* **35**, 247–250 (1975). doi:10.1103/PhysRevLett.35.247
17. A. A. Yakovenko, J. H. Reibenspies, N. Bhuvanesh, H.-C. Zhou, Generation and applications of structure envelopes for porous metal-organic frameworks. *J. Appl. Crystallogr.* **46**, 346–353 (2013).

18. L. H. Wee, M. R. Lohe, N. Janssens, S. Kaskel, J. A. Martens, Fine tuning of the metal–organic framework $Cu_3(BTC)_2$ HKUST-1 crystal size in the 100 nm to 5 micron range. *J. Mater. Chem.* **22**, 13742 (2012).

19. B. S. Brunschwig, C. Creutz, N. Sutin, Optical transitions of symmetrical mixed-valence systems in the Class II–III transition regime. *Chem. Soc. Rev.* **31**, 168–184 (2002).

20. S. Matsuzaki, R. Kuwata, K. Toyoda, Raman spectra of conducting TCNQ salts; Estimation of the degree of charge transfer from vibrational frequencies. *Solid State Commun.* **33**, 403–405 (1980).

21. J. S. Chappell, A. N. Bloch, W. A. Bryden, M. Maxfield, T. O. Poehler, D. O. Cowan, Degree of charge transfer in organic conductors by infrared absorption spectroscopy. *J. Am. Chem. Soc.* **103**, 2442–2443 (1981).

22. G. Inzelt, R. W. Day, J. F. Kinstle, J. O. Chambers, Electrochemistry and electron spin resonance of tetracyanoquinodimethane modified electrodes. Evidence for mixed-valence radical anions in the reduction process. *J. Phys. Chem.* **87**, 4592–4598 (1983).

23. M. C. Biesinger, L. W. M. Lau, A. R. Gerson, R. S. C. Smart, Resolving surface chemical states in XPS analysis of first row transition metals, oxides and hydroxides: Sc, Ti, V, Cu and Zn. *Appl. Surf. Sci.* **257**, 887–898 (2010).

24. M. Valiev, E. J. Bylaska, N. Govind, K. Kowalski, T. P. Straatsma, H. J. J. Van Dam, D. Wang, J. Nieplocha, E. Apra, T. L. Windus, W. A. de Jong, NWChem: A comprehensive and scalable open-source solution for large scale molecular simulations. *Comput. Phys. Commun.* **181**, 1477–1489 (2010).

25. A. D. Becke, Density-functional thermochemistry. III. The role of exact exchange. *J. Chem. Phys.* **98**, 5648 (1993).

26. A. Schäfer, H. Horn, R. Ahlrichs, Fully optimized contracted Gaussian basis sets for atoms Li to Kr. *J. Chem. Phys.* **97**, 2571 (1992

27. L. Noodleman, Valence bond description of antiferromagnetic coupling in transition metal dimers. *J. Chem. Phys.* **74**, 5737 (1981).

28. L. Noodleman, D. A. Case, Density functional theory of spin polarization and spin coupling in iron-sulfur clusters. *Adv. Inorg. Chem.* **38**, 423–470 (1992).

29. Q. Wu, T. Van Voorhis, Direct optimization method to study constrained systems within density-functional theory. *Phys. Rev. A* **72**, 024502 (2005).

30. A. Farazdel, M. Dupuis, E. Clementi, A. Aviram, Electric-field induced intramolecular electron transfer in spiro.pi.-electron systems and their suitability as molecular electronic devices. A theoretical study. *J. Am. Chem. Soc.* **112**, 4206–4214 (1990).

31. R. A. Marcus, N. Sutin, Electron transfers in chemistry and biology. *Biochim. Biophys. Acta* **811**, 265–322 (1985).

32. G. Kresse, J. Hafner, Ab initio molecular dynamics for liquid metals. *Phys. Rev. B* **47**, 558–561 (1993).

33. G. Kresse, J. Hafner, Ab initio molecular-dynamics simulation of the liquid-metal–amorphous-semiconductor transition in germanium. *Phys. Rev. B* **49**, 14251–14269 (1994).

34. G. Kresse, J. Furthmüller, Efficiency of ab-initio total energy calculations for metals and semiconductors using a plane-wave basis set. *Comput. Mater. Sci.* **6**, 15–50 (1996).

35. G. Kresse, J. Furthmüller, Efficient iterative schemes for ab initio total-energy calculations using a plane-wave basis set. *Phys. Rev. B* **54**, 11169–11186 (1996).

36. J. P. Perdew, A. Ruzsinszky, G. I. Csonka, O. A. Vydrov, G. E. Scuseria, L. A. Constantin, X. Zhou, K. Burke, Restoring the density-gradient expansion for exchange in solids and surfaces. *Phys. Rev. Lett.* **100**, 136406 (2008).

37. P. E. Blöchl, Projector augmented-wave method. *Phys. Rev. B* **50**, 17953–17979 (1994).

38. G. Kresse, D. Joubert, From ultrasoft pseudopotentials to the projector augmented-wave method. *Phys. Rev. B* **59**, 1758–1775 (1999).

39. A. Bencini, C. Benelli, D. Gatteschi, C. Zanchini, EPR as a necessary complement of magnetic measurements in exchange coupled systems. *Proc. Ind. Acad. Sci. Chem. Sci.* **98**, 13–22